I-MedSAM: Implicit Medical Image Segmentation with Segment Anything

Xiaobao Wei^{1,2*}, Jiajun Cao^{3,7*}, Yizhu Jin^{4,7}, Ming Lu^{5,7},
Guangyu Wang⁶, Shanghang Zhang^{7†}

¹Institute of Software, Chinese Academy of Sciences

²University of Chinese Academy of Sciences

³Xi'an Jiaotong University ⁴Beihang University ⁵Intel Labs China

⁶Beijing University of Posts and Telecommunications ⁷Peking University

weixiaobao23@mails.ucas.ac.cn

Abstract

With the development of Deep Neural Networks (DNNs), many efforts have been made to handle medical image segmentation. Traditional methods such as nnUNet train specific segmentation models on the individual datasets. Plenty of recent methods have been proposed to adapt the foundational Segment Anything Model (SAM) to medical image segmentation. However, they still focus on discrete representations to generate pixel-wise predictions, which are spatially inflexible and scale poorly to higher resolution. In contrast, implicit methods learn continuous representations for segmentation, which is crucial for medical image segmentation. In this paper, we propose I-MedSAM, which leverages the benefits of both continuous representations and SAM, to obtain better cross-domain ability and accurate boundary delineation. Since medical image segmentation needs to predict detailed segmentation boundaries, we designed a novel adapter to enhance the SAM features with high-frequency information during Parameter Efficient Fine Tuning (PEFT). To convert the SAM features and coordinates into continuous segmentation output, we utilize Implicit Neural Representation (INR) to learn an implicit segmentation decoder. We also propose an uncertainty-guided sampling strategy for efficient learning of INR. Extensive evaluations on 2D medical image segmentation tasks have shown that our proposed method with only 1.6M trainable parameters outperforms existing methods including discrete and continuous methods. The code will be released.

1. Introduction

Medical image segmentation, as a pivotal component of auxiliary disease diagnosis, holds a crucial role in medical

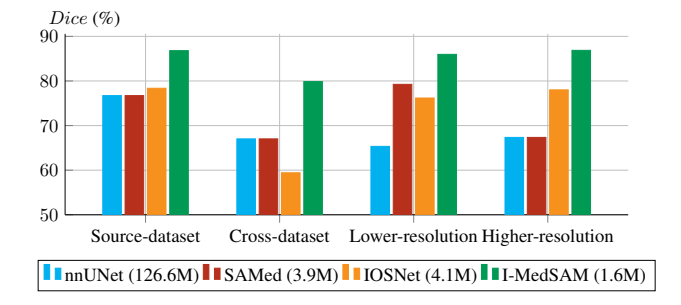


Figure 1. Segmentation quality comparison between I-MedSAM and baselines on different experiment settings. I-MedSAM with the fewest trainable params (1.6M) surpasses the state-of-the-art discrete and continuous methods and exhibits a solid generalization ability when facing data shifts.

image applications. The advent of deep learning has spurred the widespread adoption of neural networks customized for medical images. For example, nnUNet [31] leverages the downsampling and upsampling modules to aggregate multiscale contextual features. Transformers [34] uses the self-attention mechanism to significantly augment the representation capacity of deep neural networks, improving the accuracy in medical image segmentation [3]. Recent advancements have witnessed the integration of foundation models as backbones in various works. The Segment Anything Model (SAM) [18] demonstrates unprecedented zero-shot segmentation ability. Therefore, diverse adapters based on PEFT are crafted to fine-tune SAM for medical images [22, 35, 36, 39].

Despite their notable effectiveness, these methods primarily focus on pixel-wise or voxel-wise predictions [5, 8, 13, 22, 31, 39]. While they achieve promising results, the discrete representations present challenges in spatial flexibility and introduce discretization artifacts when scaling to arbitrary input sizes. Additionally, the discrete representations give rise to ambiguity when extracting the nuanced

^{*}Equal Contribution.

[†]Corresponding Author.

details crucial for precise boundary delineation [24], which is important in medical image analysis. The delineation of boundaries can signify the transitions between different human tissues or anatomical structures, thus providing essential information for accurately separating these instances. Usually, the intricacy and subtlety of this delineation process need additional refinement or supplementation [1, 27].

Compared with discrete representations, continuous representations learn Implicit Neural Representations (INRs) [25] to transform discrete representations into continuous space. Numerous approaches learn a mapping from encoded image features and grid coordinates to the segmentation output, enabling adaptability to various input resolutions [16, 26, 30, 42]. However, current approaches show unsatisfying domain transfer ability due to the limited representation capabilities of their pre-trained image encoders. Additionally, the boundary information of images demonstrates a strong correlation with features in the frequency domain [6, 20], which is also ignored by most previous methodologies. Lastly, existing methods adopt random sampling across coordinates, underestimating the influence of sampling strategies when learning INRs.

To address the aforementioned limitations, we propose I-MedSAM, a model that leverages the benefits of both continuous representations and SAM, aiming to enhance crossdomain capabilities and achieve precise boundary delineation. Given the medical images, I-MedSAM extracts the features from SAM with the proposed frequency adapter, which aggregates high-frequency information from the frequency domain. These features along with the grid coordinates are decoded into segmentation outputs by the learned INRs. We employ a two-stage implicit segmentation decoder, consisting of two INRs in a coarse-to-fine manner. The first INR produces coarse segmentation results and features. Subsequently, a novel uncertainty-guided sampling strategy is applied to sample Top-K variance feature points along with their corresponding grid coordinates. Finally, these selected samples are fed into the second INR to obtain refined segmentation results. Notably, I-MedSAM is trained end-to-end with a minimal number of trainable parameters, yet it achieves state-of-the-art performance compared with all baseline methods. Our main contributions are summarized as follows:

- We propose I-MedSAM, a novel method that leverages the advantages of SAM and continuous representations. For accurate segmentation boundaries, we design a novel frequency adapter to enhance features with high-frequency information.
- We propose a novel coarse-to-fine INR decoder with an uncertainty-guided sampling strategy, to learn a mapping from features and coordinates to segmentation output.
- We perform detailed evaluations of I-MedSAM on 2D medical image segmentation. I-MedSAM outperforms

state-of-the-art implicit and discrete methods. Experiments also demonstrate that I-MedSAM is robust to scale and domain shifts.

2. Related Work

Implicit Neural Representation. The concept of signal representation is fundamental across various domains, especially in the field of computer vision [24, 25]. Traditional methods for encoding signals discretize the input space into pixel or voxel grids [5, 10, 13, 31]. Different from these discrete methods, Implicit Neural Representation (INR) learns generator functions that map input coordinates into the signal values [4]. Numerous studies employ INR for diverse tasks, including medical data reconstruction, rendering, compression, registration, and segmentation [25]. For segmentation, conventional methods typically consist of a trained feature encoder and a decoder. The encoder encodes medical data into features, and the decoder subsequently decodes features along with their coordinates into segmentation output [12, 16, 17, 30, 32, 42]. However, current methods exhibit an imbalance in emphasizing either global or local features and demonstrate relatively low outof-distribution ability. In contrast, our proposed approach leverages the segmentation foundation model SAM to enrich feature extraction. Moreover, we introduce an innovative uncertainty-guided sampling strategy, enabling the adaptive selection of samples to train the implicit segmentation decoder.

Spectral Representation. In the context of medical image analysis, the emphasis on textual information over edge information aligns with findings that deep neural networks tend to bias towards learning low-frequency representations [24, 29]. To better leverage high-frequency information, numerous studies have extensively investigated the integration of spectral representation into deep neural networks, such as FFT, DCT, and Wavelet. Among these spectral representations, the FFT-based frequency representation emerges as particularly prevalent [23, 28, 38, 43]. The use of FFT-based frequency representation not only establishes a robust foundation for modeling but also facilitates various operations, harnessing the advantages of both spectral and spatial representations [33, 37]. While recent efforts have focused on developing adapters for SAM, there is a notable oversight in integrating information from the frequency domain to achieve accurate segmentation boundaries. To the best of our knowledge, we are the first to introduce an adapter for SAM that embeds frequency features, enhancing high-frequency modeling for more precise boundary delineation.

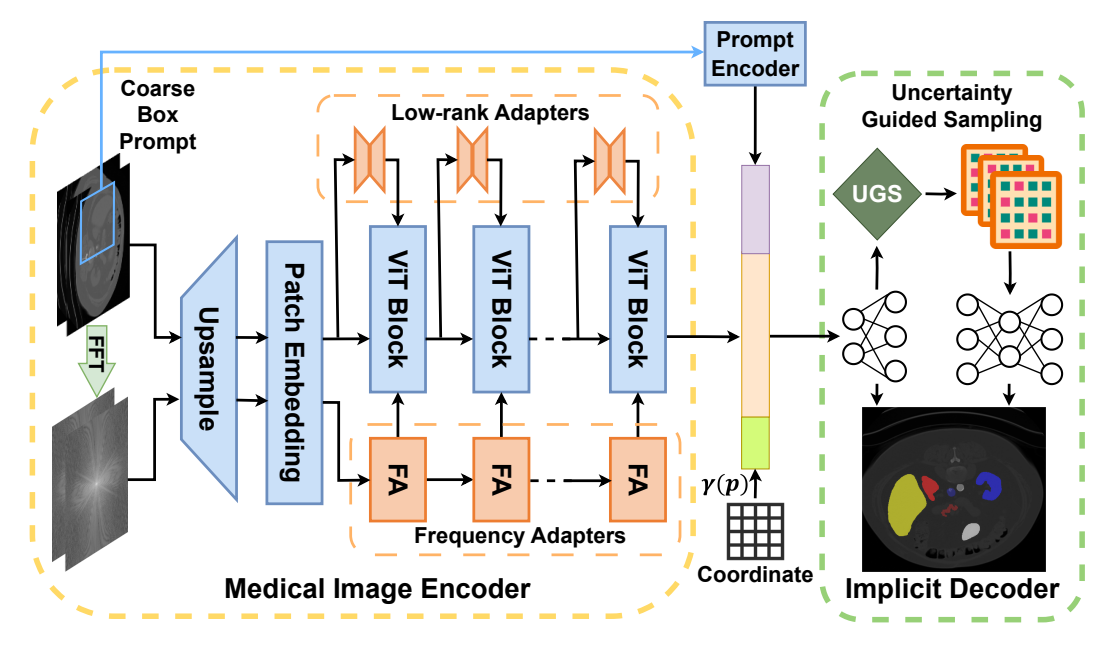


Figure 2. The overall pipeline of I-MedSAM. First, given the medical images and a coarse bounding box as a prompt, I-MedSAM utilizes the medical image encoder and the prompt encoder to generate discrete features. For the medical image encoder, we design low-rank adapters and frequency adapters to extract information from the spatial domain and frequency domain. Then I-MedSAM interpolates all features to align with the encoded coordinates and decodes them in coarse to fine neural fields. We propose an Uncertainty Guided sampling (UGS) strategy to adaptively choose the highest variance points and refine predictions. I-MedSAM merges the predictions from coarse and fine neural fields as the final prediction maps.

3. Methodology

In this section, we initially provide a concise overview of the implicit image segmentation problem. Following that, we proceed to elaborate on the pipeline of the proposed I-MedSAM. Finally, we further elucidate the novel designs introduced in I-MedSAM.

3.1. Preliminaries

In traditional discrete segmentation with C classes, neural networks aim to learn a direct mapping from input medical images $X \in \mathbb{R}^{H \times W \times 3}$ to class probabilities $O \in$ $\mathbb{R}^{H \times W \times C}$ at the same resolution. On the other hand, implicit image segmentation seeks to map each pixel of medical images X with its coordinate $p_i = (x, y)$, where $x,y \in [-1,1]$, to class probabilities $\hat{o}_i \in \mathbb{R}^C$, denoted as $\mathcal{N}_{\theta}:(p_i,X_i)\to \hat{o}_i$. Here, \mathcal{N}_{θ} represents a neural network parameterized by weights θ . This formulation integrates scale-invariant coordinates directly on pixels, adjusting the spatial granularity of input coordinates for predictions at arbitrary resolutions. Moreover, it allows the direct application of pixel-wise loss functions like Cross Entropy or Dice. Additionally, the zero-isosurface in \mathcal{N}_{θ} 's implicit space represents object boundaries, providing an additional advantage for boundary modeling.

3.2. Overall Pipeline

As depicted in Fig. 2, I-MedSAM comprises two main parts. The first part integrates an image encoder with its adapters, forming Enc_I , and a prompt encoder Enc_P , following SAM's design. Specifically, recognizing the significant role of the frequency domain in segmentation boundary representation, a frequency adapter is devised for extracting frequency features. Taken a medical image and a prompt bounding box as inputs, multi-scale features are extracted from both spatial and frequency domains. Optionally, the extracted features need to be interpolated to achieve segmentation output at desired resolution.

The second part is the implicit segmentation decoder Dec, comprising two stacked INRs: one "coarse" Dec_c with shallow layers and one "fine" Dec_f with deeper layers. Typically, Dec_c generates a coarse segmentation map, and Dec_f refines it on sampled points. The selection of these points is determined by the pixel-wise uncertainty of segmentation predictions, assessed through MC-Dropout and Top-K algorithms. Detailed explanations of these two parts will be provided in the following sections.

3.3. Medical Image Encoder

In this section, we introduce the frequency adapter and lowrank adapter integrated into SAM, to extract features from both the frequency domain and spatial domains. **Frequency Adapter.** Discrete Fourier Transform (DFT) is a common and effective method for transforming an image into the frequency domain. In practice, Fast Fourier Transform (FFT) is employed for an efficient computation of DFT, the spectrum represention of $f_{h,w}$ can be formulated as:

$$\mathcal{F}_{u,v} = \sum_{h=1}^{H} \sum_{w=1}^{W} f_{h,w} \cdot e^{-j2\pi \left(\frac{h}{H}u + \frac{w}{W}v\right)}.$$
 (1)

Subsequently, the amplitude and phase spectrum of $\mathcal{F}_{u,v}$ can be obtained as $|\mathcal{F}_{u,v}|$ and $arg(\mathcal{F}_{u,v})$, respectively. Experiment results indicate that the amplitude spectrum exhibits superior representation ability compared to the phase spectrum. Therefore, we default to using the amplitude spectrum for our proposed frequency adapter (FA).

As illustrated in Fig. 3, the individual FA comprises a linear down-projection layer, a GELU activation layer, and a linear up-projection layer. In total, we utilize n instances of FA as a sequence, corresponding to the number of Vision Transformer (ViT) Blocks of Enc_I .

Low-Rank Adapter. In contrast to fine-tuning all parameters in the image encoder Enc_I , we leverage the Low-Rank Adapter (LoRA) [11] to update a small fraction of parameters, adapting SAM to medical images, as illustrated in Fig. 3. Given the encoded token sequence $F \in \mathbb{R}^{B \times N \times C_{in}}$, the resulting token sequence $\hat{F} \in \mathbb{R}^{B \times N \times C_{out}}$ is generated using a projection layer $W \in \mathbb{R}^{C_{out} \times C_{in}}$, denoted as $\hat{F} = WF$. LoRA proposes that the adjustment to W should be gradual and consistent. It recommends utilizing a low-rank approximation $A \in \mathbb{R}^{r \times C_{in}}$ and $B \in \mathbb{R}^{C_{out} \times r}$ to represent this gradual update, formulated as:

$$\hat{W} = W + \Delta W = W + BA. \tag{2}$$

As the multi-head attention mechanism determines the regions to focus on, it is reasonable to apply LoRA to the frozen projection layers of query, key, or value to influence the attention scores. We notice that I-MedSAM performs better when LoRA is applied to the query and value projection layers, expressed as:

$$\begin{cases} Q = \hat{W}_q F = W_q F + B_q A_q F \\ K = W_k F \\ V = \hat{W}_v F = W_v F + B_v A_v F \end{cases}$$
 (3)

where W_q , W_k and W_v are freezed projection layers from SAM's image encoder, and A_q , B_q , A_v , B_v are trainable LoRA parameters.

3.4. Implicit Segmentation Decoder

In this section, we introduce implicit neural representation with an uncertainty-guided sampling strategy to decode features from encoders into segmentation maps.

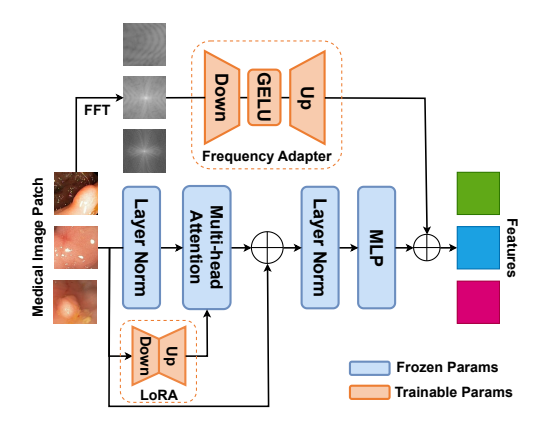


Figure 3. The illustration of the proposed frequency adapters and LoRA in the image encoder. With these adapters, I-MedSAM can be trained with minorities of parameters while obtaining high-quality segmentation boundaries.

Coarse to Fine Implicit Neural Representation. Given features from the image encoder Enc_I and the prompt encoder Enc_P , we interpolate them into the desired output resolutions and concatenate them with coordinate values p. To mitigate biased learning caused by directly using raw input coordinates [29], we map the inputs into a higher-dimensional space using a high-frequency generator function, defined as:

$$\gamma(p) = (\sin(2^{0}\pi p), \cos(2^{0}\pi p), \cdots, \\ \sin(2^{L-1}\pi p), \cos(2^{L-1}\pi p))$$
(4)

where L=10 in our experiments. The signal values from the mapped coordinates and the outputs from both the image and prompt encoders are concatenated to feed into the decoder:

$$Z^p = Concat(\gamma(p), Interp(Enc_I(X)), Enc_I(P)).$$
 (5)

Here, X and P represent the input medical image and the corresponding coarse bounding box prompt, respectively. The function Interp refers to the interpolation function based on bilinear algorithms.

Inspired by NeRF [24], we depart from the one-stage INR approaches to introduce a two-stage decoding process. This involves optimizing two INRs simultaneously: one "coarse" Dec_c , with shallow layers, and one "fine" Dec_f , with deeper layers. Dec_c produces a coarse segmentation map, \hat{o}_i^c , serving as reference for Dec_f to refine. Additionally, Dec_c generates coarse features, z_i^c , employed by Dec_f in its refinement process.

We employ MC-dropout to calculate the uncertainty of features \hat{o}_i^c for each pixel. Subsequently, a Top-K percentage of feature points, are sampled based on this uncertainty, denoted as z_i^s (with $s \in \mathcal{S}$). Finally, the predictions from the "coarse" and "fine" INRs are combined to produce the

output of I-MedSAM. The decoding process is formulated as follows:

$$\hat{o}_{i}^{c}, z_{i}^{c} = Dec_{c}(z_{i}^{p})
z_{i}^{s} = UGS(z_{i}^{c}), s \in \mathcal{S}
\hat{o}_{i}^{f} = Dec_{f}(z_{i}^{s})
\hat{O} = \hat{O}^{c}(\mathcal{S} \setminus s) \cup \hat{O}^{f}(s), \hat{o}_{i} \in \hat{O}.$$
(6)

Here, *UGS* represents Uncertainty Guided Sampling, which will be further illustrated in the following section.

Uncertainty Guided Sampling. In the sampling process, we select feature points that require refinement from the "coarse" INR Dec_c and feed them into the "fine" INR Dec_f , based on uncertainty estimation. Drawing inspiration from MC-Dropout methods [7, 9], we apply dropout T times to obtain T prediction results of coarse segmentation probabilities, $\{o_i^c\}_{t=1}^T$, given the input features z_i^p , denoted as $\{p_t(o_i^c|z_i^p)\}_{t=1}^T$. The uncertainty is calculated as the variance of predictions for each feature point, expressed as:

$$\begin{cases}
\mu_i = \frac{1}{T} \sum_{t=1}^{T} (p_t(o_i^c | z_i^p)) \\
u_i = \frac{1}{T} \sum_{t=1}^{T} (p_t(o_i^c | z_i^p) - \mu_i)^2.
\end{cases}$$
(7)

Subsequently, we sample the feature points with the highest Top-K percentage uncertainty to form z_i^s for Dec_f to refine. This estimation of uncertainty reflects the variation in prediction difficulty among different samples. It adaptively selects those with higher difficulty for refinement by Dec_f , achieving more accurate segmentation results. Please refer to the supplementary materials for a detailed illustration.

3.5. Training I-MedSAM

To optimize the trainable parameters of I-MedSAM, we freeze the pre-trained image encoder Enc_{P} , while only unfreezing the proposed adapters and INRs. We utilize SAM's image encoder with LoRA and our proposed frequency adapter to extract features for input medical images X, while extracting prompt features in terms of coarse bounding box P for targeted segmentation objects. Then we concatenate features along with the mapped coordinate values and decode them with the proposed two-stage INR decoder. With the coarse-to-fine INR and the uncertainty guided sampling strategy, I-MedSAM obtains the coarse and refined point-wise segmentation probabilities $\{\hat{o}_{i}^{c}, \hat{o}_{i}^{f}\}_{i \in X}$, combined as \hat{o}_{i} . For training optimization, we adopt pixel-wise segmentation loss, formulated as:

$$L_{seg}(o_i, \hat{o}_i) = 0.5 \cdot L_{ce}(o_i, \hat{o}_i) + 0.5 \cdot L_{dc}(o_i, \hat{o}_i)$$
 (8)

where L_{ce} and L_{dc} stand for Cross Entropy loss and Dice loss respectively. We apply the loss to supervise both coarse

and refined segmentation maps progressively. Within the training process, we slightly decrease weights for coarse supervision and increase weights for refined supervision until I-MedSAM converges.

4. Experiments

In this section, we present extensive experiments to evaluate the effectiveness of I-MedSAM for medical image segmentation. We first introduce the experimental settings including datasets and training details. Then we compare our method with the SOTA implicit and discrete approaches on the binary polyp segmentation [14] and multi-class organ segmentation [19] qualitatively and quantitatively. We further evaluate the performance and robustness of I-MedSAM when facing data shifts. Finally, we conduct a comprehensive ablation study to evaluate the contribution of each component. Due to space limitation, we provide more details and visualization results in the supplementary material.

4.1. Experimental Settings

Datasets. We assess the performance of our model on two distinct tasks: binary polyp segmentation and multi-class abdominal organ segmentation. For binary polyp segmentation, we conduct experiments using the challenging **Kvasir-Sessile** dataset [14], consisting of 196 RGB images of small sessile polyps. Additionally, we evaluate the generalization capability of our model by testing the pre-trained I-MedSAM directly to the **CVC-ClinicDB** dataset [2], comprising 612 images from 31 colonoscopy sequences.

For the segmentation of multi-organ, training is conducted on the **BCV** dataset [19], comprising 30 CT scans with annotations for 13 organs. Model robustness is also evaluated using the diverse CT images in **AMOS** [15] (200 training CTs, maintaining the same setup as in [41]). Since our work is dedicated to showing the effectiveness of 2D medical image segmentation, we just slice-wise segment CT data. Following the data prepossess in SwIPE[42], all datasets are divided with a train:validation:test ratio of 60:20:20, and the reported dice scores are all based on the test set.

Implementation Details. The training of I-MedSAM finetunes the encoder of SAM [18] with ViT-B as the backbone. We set LoRA ranks to 4 and utilize amplitude information in the proposed frequency adapters. For implicit segmentation decoders, we set [1024, 512] latent MLP dimensions for Dec_c and [512, 256, 256, 128] latent dimensions for Dec_f . We sample the highest uncertainty points with a proportion of 12.5% and set the dropout probabilities to 0.5. For multi-organ segmentation, we slightly modify the number of the last layer in Dec_c and Dec_f to match target segmentation classes. I-MedSAM are optimized by AdamW [21] with α =0.5, β =0.1, and λ_{ada} =5 × 10⁻⁵ for adapters in the encoder and λ_{dec} =1 × 10⁻³. For fair com-

Table 1.	Overall segmentation results versus the state-of-the-art discrete approaches and implicit approaches.	The Trainable Params
columns r	report unfrozen parameters in each method and the Dice columns report foreground-averaged scores.	

Bin	ary Polyp Segmentation		Multi-class Organ Segmentation			
Method	Trainable Params (M)↓	Dice (%)↑	Method	Trainable Params (M)↓	Dice (%)↑	
Discrete Approaches						
U-Net [31]	7.9	63.89	U-Net [31]	16.3	74.47	
PraNet [5]	30.5	82.56	UNETR [10]	92.6	81.14	
Res2UNet [8]	25.4	81.62	Res2UNet [8]	38.3	79.23	
nnUNet [13]	126.6	76.72	nnUNet [13]	126.6	78.65	
MedSAM [22]	4.1	79.66	MedSAM [22]	52.7	76.45	
SAMed [39]	3.9	79.31	SAMed [39]	5.6	26.63	
Implicit Approaches						
OSSNet [30]	5.2	76.11	OSSNet [30]	7.6	73.38	
IOSNet [16]	4.1	78.37	IOSNet [16]	6.2	76.75	
SwIPE [42]	2.7	85.05	SwIPE [42]	4.4	81.21	
I-MedSAM (ours)	1.6	86.80	I-MedSAM (ours)	3.5	83.04	

parisons, all methods are trained for 1000 epochs on the same experiment settings. The reported test dice score corresponds to the best validation epoch. Image input sizes are 384×384 for Sessile and 512×512 for each slice of BCV.

Baselines. We divide baselines into two sets: discrete approaches and implicit (continuous) approaches. Discrete approaches include U-Net [31], PraNet [5], Res2UNet [8], nnUNet [13], UNETR [10]. We also compare with Med-SAM [22] and SAMed [39], which are both based on SAM. Implicit approaches include OSSNet [30], IOSNet [16], SwIPE [42].

4.2. Quantitative Comparison

In this section, we first report the dice score compared with baselines. Then we conduct experiments across different resolutions and datasets to evaluate the robustness and generalization ability under data shifts.

Segmentation Comparison. We make a comparison with both the discrete approaches and implicit approaches in terms of trainable parameters and Dice for Polyp Sessile and CT BCV multi-organ segmentation, as demonstrated in Tab. 1. On the smaller polyp dataset, we observe notable improvements over the best-known implicit approaches (+1.75% Dice) and discrete methods (+4.24% Dice) with much fewer parameters (5% of PraNet [5] and 39% of IOSNet [16]). For multi-organ segmentation on BCV, the performance gains are not so significant, however, we still outperform UNETR [10] with over 30x fewer parameters. On one hand, SAM with the proposed frequency adapters generates abundant features, which boosts the quality of segmentation boundaries. On the other hand,

Table 2. Robustness for across resolutions on Kvasir-Sessile dataset.

	اد ما	Dice (%)↑				
Method		384 → 128	$384 \rightarrow 896$			
	Discrete Approaches					
PraNet	[5]	68.79	43.92			
nnUNet	[13]	65.34	67.35			
MedSAM	[22]	77.96	80.00			
SAMed [39]		79.25	79.30			
Implicit Approaches						
IOSNet	[16]	76.18	78.01			
SwIPE	[42]	81.26	84.33			
I-MedSA	M (ours)	85.97	86.84			

with proposed uncertainty-guided sampling in neural field decoders, I-MedSAM can adaptively select and refine the highest variance pixels, which also results in more accurate segmentation maps.

Robustness under Data Shifts. We also compare the robustness across resolutions and datasets with the best discrete and implicit methods on binary polyp segmentation. First, with I-MedSAM pre-trained in the standard 384×384 image size, we adjust the output resolution into lower resolutions 128×128 and higher resolutions 896×896 . Then we calculate the dice scores of varying outputs. For discrete methods, since the output resolution is the same as the input images, original medical images are resized to the target

Table 3. Generalization ability for cross-domain from Kvasir to CVC binary polyp segmentation.

Method		Dice (%)		
Kvasir o CVC				
PraNet	[5]	68.37		
nnUNet	[13]	67.02		
MedSAM	[22]	69.59		
SAMed	[39]	79.06		
IOSNet	[16]	59.42		
SwIPE	[42]	70.10		
I-MedSAN	79.86			

Table 4. Generalization ability for cross-domain from BCV to AMOS liver segmentation.

Method		Dice (%)		
$BCV \rightarrow AMOS$ (liver class only)				
UNETR	[5]	81.75		
nnUNet	[13]	79.63		
MedSAM [22]		71.98		
IOSNet	[16]	79.48		
SwIPE	[42]	82.81		
I-MedSAM (ours)		86.28		

resolution and sent to these methods to generate segmentation under the target resolution. Results can be seen in Tab. 2, implicit methods demonstrate their spatial flexibility and maintain higher performances than discrete methods. Between implicit approaches, our I-MedSAM yields the best performance under different output resolutions. Thanks to the proposed frequency adapters and uncertainty-guided sampling, I-MedSAM contains a stronger continuous representation ability, which is beneficial to the requirement for arbitrary resolution predictions.

Second, we study the robustness of data shifts in the same task across datasets. For binary polyp segmentation, we pre-train methods on Kvasir-Sessile and evaluate them on CVC datasets. For multi-class abdominal organ segmentation, we pre-train methods on BCV and evaluate them on AMOS datasets with the liver class only. Results can be seen in Tab. 3 and Tab. 4. Thanks to the generalization ability of SAM, I-MedSAM outperforms the best discrete method with a dice of 79.86% and 86.28%. For more qualitative comparisons on data shifts, please refer to supplementary materials.

Table 5. Ablation study on LoRA ranks.

LoRA Ranks	8	6	4
Dice (%)	86.73	86.74	86.80

Table 6. Ablation study on Frequency Adapter (FA). In this context, FA_{pha} stands for utilizing of the phase spectrum of DFT, while FA_{amp} represents using the amplitude spectrum.

Setting	w/o FA	FA_{pha}	FA_{amp}
Dice (%)	86.19	86.67	86.80

Table 7. Ablation study on the number of sampled feature points for Uncertainty Guided Sampling (UGS). "Top-K" denotes the selection of a specified proportion, K%, from all feature points.

Setting	w/o UGS	Top-50%	Top-25%	Top-12.5%
Dice (%)	81.00	86.51	86.63	86.80

4.3. Qualitative Comparison

As shown in Fig. 4 and Fig. 5, we conduct the qualitative comparisons on datasets Kvasir-Sessile and BCV. Since SwIPE does not release code for inference, we remove it for visual comparison. We also provide input medical images and ground truth segmentation masks. From the figures, it can be witnessed that I-MedSAM obtains better segmentation boundaries. Thanks to the proposed frequency adapters and uncertainty guided sampling techniques, I-MedSAM can efficiently aggregate high-frequency information from the input, which is beneficial to the accuracy of final segmentation maps. Due to the space limitation, please refer to supplementary materials for more qualitative results.

4.4. Ablation Study

We conducted ablation studies focusing on three aspects: LoRA rank adjustment, incorporating the frequency adapter, and point numbers for sampling. In each of our ablation experiments, other hyper-parameters remain consistent with the implementation details.

LoRA Ranks. Tab. 5 illustrates the impact of different values of LoRA ranks in I-MedSAM. When LoRA ranks is set to 4, it exhibits optimal performance while minimizing training parameters. This demonstrates the effectiveness of this fine-tuning technique.

Frequncy adapter components. Tab. 6 indicates the effectiveness of the frequency adapter, and it can be observed that amplitude information is more helpful for spectrum representation compared to phase information. Thus our proposed frequency adapters fully take advantage of amplitude information, which is more related to segmentation boundaries.

Points Number for Sampling. Tab. 7 represents ab-

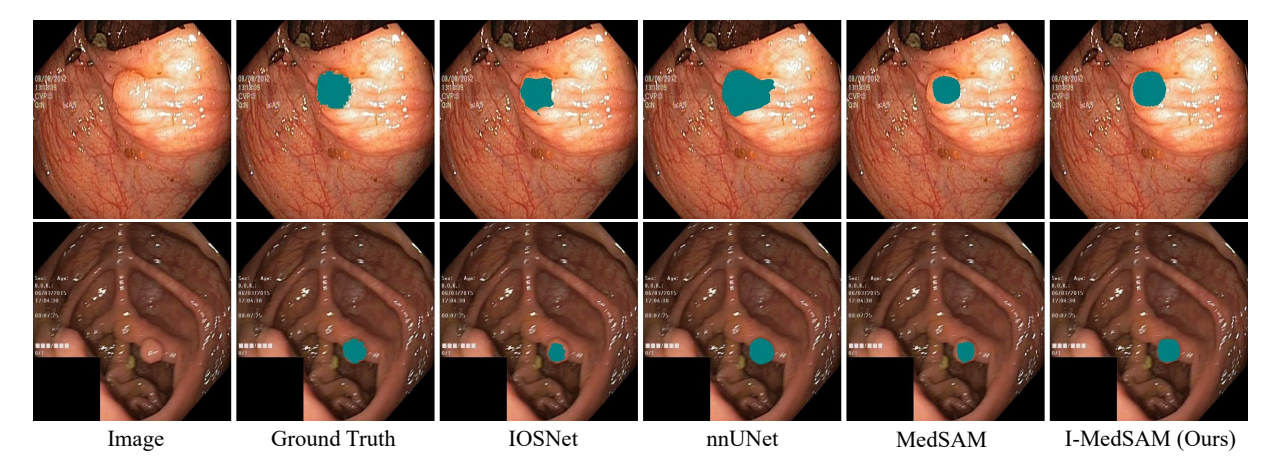


Figure 4. Qualitative comparison on Kvasir-Sessile dataset for binary polyp segmentation. Best viewed in colors.

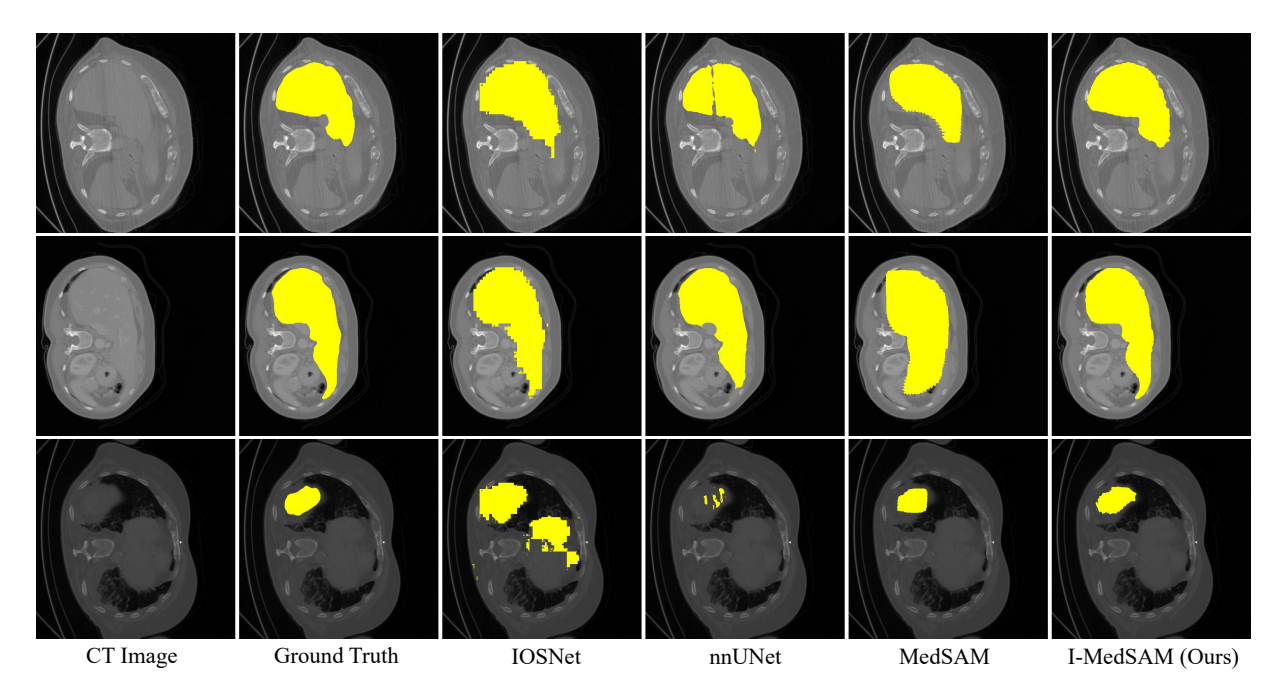


Figure 5. Qualitative comparison on BCV dataset for liver segmentation. Best viewed in colors.

lation on points number for Uncertainty Guided Sampling (UGS). This experiment reveals that I-MedSAM generates high-quality segmentation masks with the help of the proposed uncertainty guided sampling method. However enormous sampling points do not contribute to final segmentation and introduce additional memory consumption. Thus a proportion of 12.5% for UGS is sufficient for I-MedSAM.

5. Limitation

While SAM has been equipped with various adapters to address diverse tasks, the simultaneous handling of medical images from multiple domains, including MRI and CT, remains a formidable challenge in the field of medical image

processing [40]. A potential strategy for improvement is the extension of I-MedSAM with a more universal adapter capable of generalizing across different modalities. Despite these challenges, I-MedSAM has effectively showcased the utility of leveraging Implicit Neural Representations (INRs) to enhance SAM's adaptability, demonstrating promising outcomes in aligning with out-of-distribution data for specific tasks.

6. Conclusion

In this paper, we introduce I-MedSAM to enhance crossdomain ability and adaptability to diverse input resolutions in medical image segmentation. By integrating SAM's generalized representations into the INR space, I-MedSAM achieves state-of-the-art performance across various experimental scenarios. Specifically addressing the challenge of precise boundary delineation in 2D medical images, we incorporate a frequency adapter for parameter-efficient finetuning to SAM, showcasing the potential benefits of complementing spatial domain information with frequency domain insights for foundation models. Additionally, the employment of the uncertainty-guided sampling strategy in coarse-to-fine INRs proves effective in the selection and refinement of challenging samples in continuous space. These findings suggest avenues for future research to establish stronger connections between different representation spaces.

References

- [1] Mohammad D Alahmadi. Boundary aware u-net for medical image segmentation. *Arabian Journal for Science and Engineering*, 48(8):9929–9940, 2023. 2
- [2] Jorge Bernal, F Javier Sánchez, Gloria Fernández-Esparrach, Debora Gil, Cristina Rodríguez, and Fernando Vilariño. WM-DOVA maps for accurate polyp highlighting in colonoscopy: Validation vs. saliency maps from physicians. Computerized Medical Imaging and Graphics, 43:99–111, 2015. 5
- [3] Jieneng Chen, Yongyi Lu, Qihang Yu, Xiangde Luo, Ehsan Adeli, Yan Wang, Le Lu, Alan L Yuille, and Yuyin Zhou. Transunet: Transformers make strong encoders for medical image segmentation. *arXiv preprint arXiv:2102.04306*, 2021. 1
- [4] Julian Chibane, Thiemo Alldieck, and Gerard Pons-Moll. Implicit functions in feature space for 3d shape reconstruction and completion. In Proceedings of the IEEE/CVF conference on computer vision and pattern recognition, pages 6970–6981, 2020.
- [5] D.P. Fan, G.P. Ji, T. Zhou, G. Chen, H.Z. Fu, J.B. Shen, and L. Shao. PraNet: Parallel reverse attention network for polyp segmentation. In *MICCAI*, pages 263–273. Springer, 2020. 1, 2, 6, 7
- [6] Zhenghao Feng, Lu Wen, Peng Wang, Binyu Yan, Xi Wu, Jiliu Zhou, and Yan Wang. Diffdp: Radiotherapy dose prediction via a diffusion model. In *International Conference* on Medical Image Computing and Computer-Assisted Intervention, pages 191–201. Springer, 2023. 2
- [7] Yarin Gal and Zoubin Ghahramani. Dropout as a bayesian approximation: Representing model uncertainty in deep learning. *international conference on machine learning*, 2015. 5
- [8] Shang-Hua Gao, Ming-Ming Cheng, Kai Zhao, Xin-Yu Zhang, Ming-Hsuan Yang, and Philip Torr. Res2Net: A new multi-scale backbone architecture. *IEEE TPAMI*, 43(2):652–662, 2019. 1, 6
- [9] Chuan Guo, Geoff Pleiss, Yu Sun, and Kilian Q. Weinberger. On calibration of modern neural networks. *international conference on machine learning*, 2017.

- [10] A. Hatamizadeh, Y. Tang, V. Nath, D. Yang, A. Myronenko, B. Landman, H.R. Roth, and D. Xu. UNETR: Transformers for 3D medical image segmentation. In *IEEE/CVF Win*ter Conference on Applications of Computer Vision (WACV), pages 574–584, 2022. 2, 6
- [11] Edward J Hu, Yelong Shen, Phillip Wallis, Zeyuan Allen-Zhu, Yuanzhi Li, Shean Wang, Lu Wang, and Weizhu Chen. Lora: Low-rank adaptation of large language models. arXiv preprint arXiv:2106.09685, 2021. 4
- [12] H. Hu, Y. Chen, J. Xu, S. Borse, H. Cai, F. Porikli, and X. Wang. Learning implicit feature alignment function for semantic segmentation. In *ECCV*, pages 487–505. Springer, 2022. 2
- [13] F. Isensee, P.F. Jaeger, S.AA Kohl, J. Petersen, and K. H. Maier-Hein. nnU-Net: A self-configuring method for deep learning-based biomedical image segmentation. *Nature Methods*, 18(2):203–211, 2021. 1, 2, 6, 7
- [14] Debesh Jha, Pia H Smedsrud, Dag Johansen, Thomas de Lange, Håvard D Johansen, Pål Halvorsen, and Michael A Riegler. A comprehensive study on colorectal polyp segmentation with ResUNet++, conditional random field and testtime augmentation. *IEEE Journal of Biomedical and Health Informatics*, 25(6):2029–2040, 2021. 5
- [15] Y. Ji, H. Bai, J. Yang, C. Ge, Y. Zhu, R. Zhang, Z. Li, L. Zhang, W. Ma, X. Wan, et al. AMOS: A large-scale abdominal multi-organ benchmark for versatile medical image segmentation. *ArXiv*:2206.08023, 2022. 5
- [16] M.O. Khan and Y. Fang. Implicit neural representations for medical imaging segmentation. In MICCAI, 2022. 2, 6, 7
- [17] Muhammad Osama Khan and Yi Fang. Implicit neural representations for medical imaging segmentation. In International Conference on Medical Image Computing and Computer-Assisted Intervention, pages 433–443. Springer, 2022. 2
- [18] Alexander Kirillov, Eric Mintun, Nikhila Ravi, Hanzi Mao, Chloe Rolland, Laura Gustafson, Tete Xiao, Spencer Whitehead, Alexander C Berg, Wan-Yen Lo, et al. Segment anything. arXiv preprint arXiv:2304.02643, 2023. 1, 5
- [19] Bennett Landman, Zhoubing Xu, J Igelsias, Martin Styner, T Langerak, and Arno Klein. Miccai multi-atlas labeling beyond the cranial vault-workshop and challenge. In Proc. MICCAI Multi-Atlas Labeling Beyond Cranial Vault-Workshop Challenge, page 12, 2015. 5
- [20] Yunxiang Li, Hua-Chieh Shao, Xiao Liang, Liyuan Chen, Ruiqi Li, Steve Jiang, Jing Wang, and You Zhang. Zeroshot medical image translation via frequency-guided diffusion models. arXiv preprint arXiv:2304.02742, 2023. 2
- [21] Ilya Loshchilov and Frank Hutter. Decoupled weight decay regularization. In *ICLR*, 2017. 5
- [22] Jun Ma and Bo Wang. Segment anything in medical images. arXiv preprint arXiv:2304.12306, 2023. 1, 6, 7
- [23] Xintian Mao, Yiming Liu, Fengze Liu, Qingli Li, Wei Shen, and Yan Wang. Intriguing findings of frequency selection for image deblurring. In *Proceedings of the AAAI Conference on Artificial Intelligence*, pages 1905–1913, 2023. 2
- [24] Ben Mildenhall, Pratul P Srinivasan, Matthew Tancik, Jonathan T Barron, Ravi Ramamoorthi, and Ren Ng. Nerf:

- Representing scenes as neural radiance fields for view synthesis. *Communications of the ACM*, 65(1):99–106, 2021. 2,
- [25] Amirali Molaei, Amirhossein Aminimehr, Armin Tavakoli, Amirhossein Kazerouni, Bobby Azad, Reza Azad, and Dorit Merhof. Implicit neural representation in medical imaging: A comparative survey. In Proceedings of the IEEE/CVF International Conference on Computer Vision, pages 2381– 2391, 2023. 2
- [26] Sergio Naval Marimont and Giacomo Tarroni. Implicit field learning for unsupervised anomaly detection in medical images. In Medical Image Computing and Computer Assisted Intervention–MICCAI 2021: 24th International Conference, Strasbourg, France, September 27–October 1, 2021, Proceedings, Part II 24, pages 189–198. Springer, 2021. 2
- [27] Anitha Pasupathy. The neural basis of image segmentation in the primate brain. *Neuroscience*, 296:101–109, 2015.
- [28] Anish Prabhu, Ali Farhadi, Mohammad Rastegari, et al. Butterfly transform: An efficient fft based neural architecture design. In Proceedings of the IEEE/CVF Conference on Computer Vision and Pattern Recognition, pages 12024–12033, 2020.
- [29] Nasim Rahaman, Aristide Baratin, Devansh Arpit, Felix Draxler, Min Lin, Fred Hamprecht, Yoshua Bengio, and Aaron Courville. On the spectral bias of neural networks. In *International Conference on Machine Learning*, pages 5301–5310. PMLR, 2019. 2, 4
- [30] C. Reich, T. Prangemeier, O. Cetin, and H. Koeppl. OSS-Net: Memory efficient high resolution semantic segmentation of 3D medical data. In *British Machine Vision Conference*, 2021. 2, 6
- [31] O. Ronneberger, P. Fischer, and T. Brox. U-Net: Convolutional networks for biomedical image segmentation. In *MIC-CAI*, pages 234–241. Springer, 2015. 1, 2, 6
- [32] K.S. Sørensen, O. Camara, O.D. Backer, K.F. Kofoed, and R.R. Paulsen. NUDF: Neural unsigned distance fields for high resolution 3D medical image segmentation. *ISBI*, pages 1–5, 2022. 2
- [33] Xianlun Tang, Jiangping Peng, Bing Zhong, Jie Li, and Zhenfu Yan. Introducing frequency representation into convolution neural networks for medical image segmentation via twin-kernel fourier convolution. *Computer Methods and Programs in Biomedicine*, 205:106110, 2021. 2
- [34] Ashish Vaswani, Noam Shazeer, Niki Parmar, Jakob Uszkoreit, Llion Jones, Aidan N Gomez, Łukasz Kaiser, and Illia Polosukhin. Attention is all you need. Advances in neural information processing systems, 30, 2017.
- [35] Xiaobao Wei, Renrui Zhang, Jiarui Wu, Jiaming Liu, Ming Lu, Yandong Guo, and Shanghang Zhang. Noc: High-quality neural object cloning with 3d lifting of segment anything. *arXiv preprint arXiv:2309.12790*, 2023. 1
- [36] Junde Wu, Rao Fu, Huihui Fang, Yuanpei Liu, Zhaowei Wang, Yanwu Xu, Yueming Jin, and Tal Arbel. Medical sam adapter: Adapting segment anything model for medical image segmentation. arXiv preprint arXiv:2304.12620, 2023.
- [37] Zhi-Qin John Xu, Yaoyu Zhang, and Yanyang Xiao. Training behavior of deep neural network in frequency domain. In

- Neural Information Processing: 26th International Conference, ICONIP 2019, Sydney, NSW, Australia, December 12–15, 2019, Proceedings, Part I 26, pages 264–274. Springer, 2019. 2
- [38] Dafeng Zhang, Jia Ouyang, Guanqun Liu, Xiaobing Wang, Xiangyu Kong, and Zhezhu Jin. Ff-former: Swin fourier transformer for nighttime flare removal. In *Proceedings of* the IEEE/CVF Conference on Computer Vision and Pattern Recognition, pages 2823–2831, 2023. 2
- [39] Kaidong Zhang and Dong Liu. Customized segment anything model for medical image segmentation. *arXiv preprint arXiv:2304.13785*, 2023. 1, 6, 7
- [40] Yichi Zhang and Rushi Jiao. How segment anything model (sam) boost medical image segmentation? arXiv preprint arXiv:2305.03678, 2023. 8
- [41] Yejia Zhang, Nishchal Sapkota, Pengfei Gu, Yaopeng Peng, Hao Zheng, and Danny Z Chen. Keep your friends close & enemies farther: Debiasing contrastive learning with spatial priors in 3D radiology images. In 2022 IEEE International Conference on Bioinformatics and Biomedicine (BIBM), pages 1824–1829. IEEE, 2022. 5
- [42] Yejia Zhang, Pengfei Gu, Nishchal Sapkota, and Danny Z Chen. Swipe: Efficient and robust medical image segmentation with implicit patch embeddings. In *International Conference on Medical Image Computing and Computer-Assisted Intervention*, pages 315–326. Springer, 2023. 2, 5, 6, 7
- [43] Qiang Zhu, Pengfei Li, and Qianhui Li. Attention retractable frequency fusion transformer for image super resolution. In *Proceedings of the IEEE/CVF Conference on Computer Vision and Pattern Recognition*, pages 1756–1763, 2023. 2